

# CFD VALIDATION OF MICRO HOVERING ROTOR IN GROUND EFFECT

Tarandeep S. Kalra \*

Vinod K. Lakshminarayan †

James D. Baeder ‡

Alfred Gessow Rotorcraft Center  
Department of Aerospace Engineering  
University of Maryland  
College Park, MD 20742.

## Abstract

A compressible, structured, overset Reynolds Averaged Navier Stokes (RANS) solver is used to simulate a micro-hovering rotor in ground effect (IGE) to demonstrate the capability of the code to provide accurate tip vortex flow-field predictions, and provide a good understanding of the ground-wake interactions in conditions prevalent in helicopter brownout. The performance validation at various ground distances shows good correlation with the experimental thrust and power measurements. Further, detailed comparisons of the predicted tip vortex flow-field obtained by comparing vorticity contours and radial velocity profiles with the experimental PIV measurements show very good agreement. The examination of the IGE tip-vortex flow-field suggests a greater degree of unsteadiness with decreasing rotor distance above ground. Analysis of the velocity vectors and the eddy viscosity contours near the ground indicate that the flow near the ground is mostly laminar. However, the induced velocities arising from the proximity of the rotor tip vortices cause the boundary layer to become more turbulent. With decreasing rotor height above ground, the increased interactions between the tip vortices and the ground boundary layer result in intermixing of eddy viscosity from the tip vortex to the ground boundary layer. The presence of laminar separation is evident at smaller rotor heights above ground. The use of negative twist on the blade results in further destabilization of the tip vortices due to increased vortex-vortex interactions.

## Nomenclature

|            |   |
|------------|---|
| $A$        | Area of the rotor blades ( $\pi R^2$ ), $m^2$   |
| $c$        | Blade chord, m  |
| $C_T$      | Thrust coefficient = Thrust/ $(\rho\pi R^2 U_{tip}^2)$  |
| $C_P$      | Power coefficient = Power/ $(\rho\pi R^2 U_{tip}^3)$  |
| $h$        | Rotor height above ground, m  |
| $M_{tip}$  | Tip Mach number   |
| $q$        | non-dimensionalized second invariant of the velocity gradient tensor, $\frac{\partial u_i}{\partial x_j} \frac{\partial u_j}{\partial x_i}$ (normalized by tip speed and blade chord) |
| $r$        | Radial distance, m  |
| $R$        | Radius of the rotor, m  |
| $Re$       | Reynolds number   |
| $U_{tip}$  | Tip speed, m/s  |
| $z$        | Distance above the ground, m  |
| $\theta_o$ | Collective pitch, degrees   |
| $\Psi$     | Wake age, degrees   |

## Introduction

One of the serious problems associated with helicopters operating in desert or dusty environment is the ‘brownout’ condition. When the helicopter operates at close proximity to the ground, dust particles from the ground get entrained into the air. Under certain operational conditions, particularly during take off and landing, these entrained particles tend to recirculate around the helicopter to form large dust clouds. An intense dust cloud can severely obscure the pilot’s vision, which may culminate in a loss of situational awareness. In the recent past, military operations in brownout conditions have resulted in several helicopter accidents, forcing helicopter analysts to investigate the physics related to brownout, and try to develop long-term mitigation strategies.

Most of the current workarounds to the brownout problem include either the use of additional sensors to improve the visibility or to use operational tactics to avoid getting into the brownout situation. Although, these solutions help in limiting the number of mishaps caused by the brownout, it is still desirable to find a more permanent solution to this problem. Since the interaction of the rotor wake with the ground and the dust particles form the root cause of the brownout problem, it is believed that

\* Graduate Research Assistant, tkalra@umd.edu

† Research Associate, vinodkl@umd.edu

‡ Associate Professor, baeder@umd.edu

a detailed understanding of the fluid physics along with a good knowledge of the fluid-particle interaction under these conditions can help researchers develop effective means of preventing and/or mitigating the adverse effects of rotorcraft brownout.

However, there are numerous challenges associated with studying the brownout phenomena. The most important challenge comes from the enormity of the problem, which needs to be tackled over a wide range of flight conditions and sizes of dust particles over different terrains. In addition, photographic evidence shows that different helicopters with distinct design features such as blade twist, rotor disk loading, tip shape, number of blades, etc. produce different dust cloud shapes and intensities while operating in brownout condition, thus complicating the problem even further. However, this also suggests that a suitable blade design might indeed be able to prevent or mitigate the brownout problem. A good physical understanding of such an extremely challenging and multi-phase problem can only be achieved by a combined effort from the experimental and computational studies.

Although some significant progress has been made on experimental studies of the brownout problem, research is still at its early stages. The main experimental difficulty comes in simulating the various brownout conditions, especially with a full-scale helicopter rotor. To overcome the problem associated with scale, some recent experiments were performed at the University of Maryland to study the effect of ground plane (Ref. 1) and the phenomenon of particle entrainment (Ref. 2) on a hovering MAV-scale rotor. It is believed that a good amount of physical understanding of the actual brownout phenomenon can be obtained from the studies at smaller scales. Detailed PIV measurements of the flow-field were performed in Ref.1. The study showed competing phenomenon of vortex stretching, diffusion and turbulence generated at the ground. In addition, vortex pairing was seen to induce stronger velocities near the ground. In Ref.2, PIV measurements were used to study the lift-off and the entrainment of sediment particles. The development of the wall jet within the boundaries of the rotor wake and the ground plane was observed to aid the sediment particles to attain their threshold velocities for lift off from the ground. Currently, similar experiments are being performed on a sub-scale rotor at the University of Maryland to gain further understanding of the physics. Other experimental studies include the work of Nathan and Green (Ref. 3), who performed PIV measurements and experimental brownout simulations. Experiments were conducted in a wind tunnel to simulate low speed forward flight on a micro-scale rotor. These results showed an increase in dust pickup with increasing advance ratios.

In comparison to the experiments, computational studies can easily simulate a wide range of brownout conditions. However, there are several challenges associated with the computational studies such as:

- The tip vortex emanating from the blade needs to be preserved for a significantly long time to capture the interaction with the ground, and therefore, can be computationally expensive, especially when the ground distances are large.
- It is necessary to resolve the boundary layer and the turbulence at the ground, which can be extremely challenging especially using non-CFD computational methods.
- Modeling the fluid-particle interaction for these complicated flow-field is extremely challenging. Development of a particle model is still an active field of research.

To simplify the computations, most recent studies simplify the multi-phase brownout problem by ignoring the effects of the airborne sediment particles on the flow-field. This decoupled approach allows one to concentrate on the problem of tracking the generation, evolution of the rotor tip vortices and its interaction with the ground boundary layer. Ignoring the effect of sediment particles on the rotor IGE aerodynamic environment might not be valid under all brownout conditions. However, this still serves as a good first level approximation that can provide the much needed insight into the flow-field associated with a rotor operating IGE. The current paper focuses on the first part of the problem by trying to accurately compute the rotor wake and its interaction with the ground. The various physical phenomenon that needs to be captured in the current work is shown in the schematic, see Fig. 1. The schematic shows tip vortices shed from the rotor blade, which expands near the ground to form

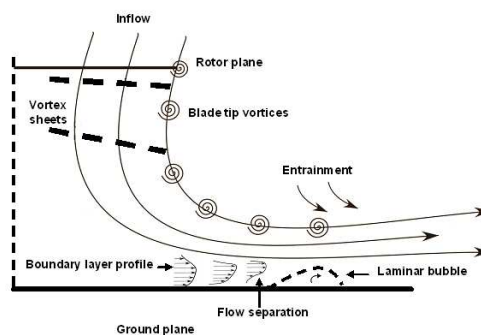
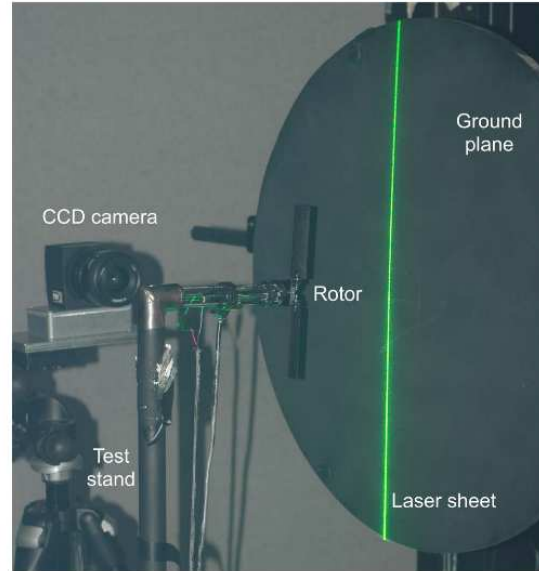


Figure 1: Schematic of the flow-field for a rotor operating in ground effect.

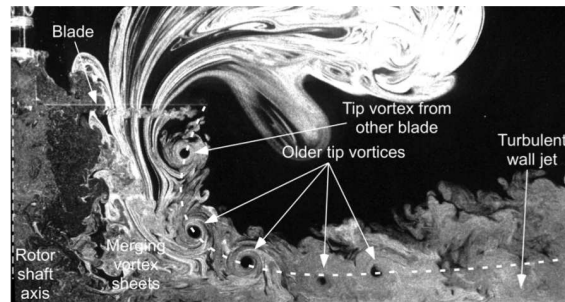
a jet flow. The flow developed near the ground can separate and form separation bubble under adverse pressure gradients.

Currently, most approaches track the tip vortex in the particle-fixed Lagrangian frame of reference (Refs. 4, 5). Even though the free-vortex type methods can track the vortex for a very long distance, these methods involve certain degree of empiricism in determining the vortex core radius and roll-up. In addition, they also need to rely on approximate sublayer models to predict the ground boundary layer. Therefore, these methods may only be able to provide a qualitative prediction of the particle entrainment. Methods using Vorticity Transport Model (VTM) (Ref. 6) or vorticity confinement (Ref. 7) provide better representation of the tip vortex. However, VTM is an inviscid model and still requires approximate sublayer models to capture ground boundary layer. On the other hand, vorticity confinement methods uses empirical factors that may not be easily determined in a ground plane simulations.

A RANS-based CFD approach can resolve velocities near the ground without the use of any empirical factors or sublayer models. Therefore, it does not suffer from the problems associated with the other models. However, these methods are considerably more expensive compared to the other models. By taking advantage of the advances in computing technologies, and through effective use of parallelization techniques, one can use these high fidelity methods to simulate brownout problems. The current work demonstrates the use of a compressible Reynold-averaged Navier-Stokes (RANS) solver to accurately simulate a rotor in ground-effect. The high resolution flow-field measurement of hovering micro-rotor experiments performed by Lee et al. (Ref. 1) is used for validation. An earlier work by Lakshminarayan and Baeder (Ref. 8) showed the capability of this solver to provide accurate performance and flow-field characteristics of the rotor tested by Lee et al. in out-of-ground condition. The current work extends this work to simulate the rotor in-ground effect. Following the performance comparison with experimental data, the velocity field for various rotor heights above ground are compared with the experimental PIV results. Additional analysis is performed to understand the details of flow physics very close to the ground, where experimental measurement is extremely challenging. In addition, a preliminary study is performed to understand the effect of using twisted blade at one particular rotor height above ground. Note that the solutions obtained from the current simulations can be provided to a sediment tracking code to simulate the full brownout problem.



(a) Experimental setup



(b) Experimental flow visualization

Figure 2: Experimental setup and flow visualization (Ref. 1).

## Experimental Setup for Validation

As mentioned before, experimental setup of Lee et al. (Ref. 1) is used for validating the flow-field predicted of a rotor operating in-ground effect. The setup consists of a 2-bladed hovering rotor in which the rotor tip-path-plane was set parallel to a ground plane, see Fig. 2(a). The blades are rectangular and untwisted with an aspect ratio of 4.39. The blades have a circular arc airfoil with 3.7% thickness and 3.3% camber. The rotor was operated at a constant collective pitch  $\theta_o = 12^\circ$ . The experimental results were obtained at a root Reynolds number of 6,480, a tip Reynolds number of 32,400 and a tip Mach Number of 0.08. PIV measurements were performed at different ground plane distances ranging from 0.25 to 2.5 times the rotor radius. Figure 2(b) shows a sample flow visualization obtained from the experiment. It can be seen that the experiment clearly captures various physical phenomenon mentioned in the schematic 1.

## Methodology

### Flow Solver

The computations are performed using the overset structured RANS solver OVERTURNS (Ref. 9). All the computations are performed in a time-accurate manner in the inertial frame of reference. The code solves the compressible RANS equations using a preconditioned dual-time scheme in the diagonalized approximate factorization framework, described by Buelow et al. (Ref. 11) and Pandya et al. (Ref. 12). The diagonal form of implicit approximate factorization method was originally developed by Pulliam and Chaussee (Ref. 13). The low Mach preconditioning is based on the one developed by Turkel (Ref. 14). The preconditioning is used not only to improve convergence but also to improve the accuracy of the solution. The inviscid terms are computed using a third order MUSCL scheme utilizing Koren’s limiter with Roe’s flux difference splitting and the viscous terms are computed using second order central differencing. The Spalart-Allmaras (Ref. 15) turbulence model is employed for the RANS closure. This one-equation model has the advantages of ease of implementation, computational efficiency and numerical stability. The production term in this eddy-viscosity model is modified (Ref. 16) to account for the reduction in turbulence levels at the vortex core due to rotational effects.

### Mesh System

A two mesh overset system consisting of a body conforming C-O type blade mesh and a cylindrical background mesh was used in the present study. Flow periodicity in

| $h/R$ | Mesh points                 | Total number of points<br>(in millions) |
|-------|-----------------------------|---|
| 0.25  | $187 \times 233 \times 172$ | 7.6                                     |
| 0.5   | $187 \times 233 \times 217$ | 9.1                                     |
| 1.0   | $187 \times 180 \times 304$ | 9.8                                     |
| 1.5   | $187 \times 180 \times 440$ | 14.3                                    |

Table 1: Number of mesh points used in the background mesh.

the azimuthal direction was utilized to simulate only one half of the computational domain, thereby reducing the computational cost. Information is exchanged from one grid to the other using chimera interpolations. Implicit hole-cutting technique, developed by Lee (Ref. 17) and improved by Lakshminarayan (Ref. 9), is used to determine the connectivity information between various overset meshes. The dimensions of the blade mesh in the streamwise, spanwise and normal directions are  $267 \times 93 \times 50$  points, respectively. The background meshes for all the rotor heights above ground have 187 points in the azimuthal direction, such that a grid plane is placed every  $1^\circ$  of the azimuth. The number of grid points in the radial and vertical directions of the background mesh were adjusted for different rotor heights above the ground. The background meshes for all the different rotor heights are refined to accurately resolve tip vortices all the way to the ground. In addition, the mesh is further refined near the ground to resolve the boundary layer. Table 1 tabulates the size of the background mesh used for the various rotor heights simulated above ground. Note that the rotor height from the ground is represented by the variable  $h$ . As the rotor height increases, the number of points in the

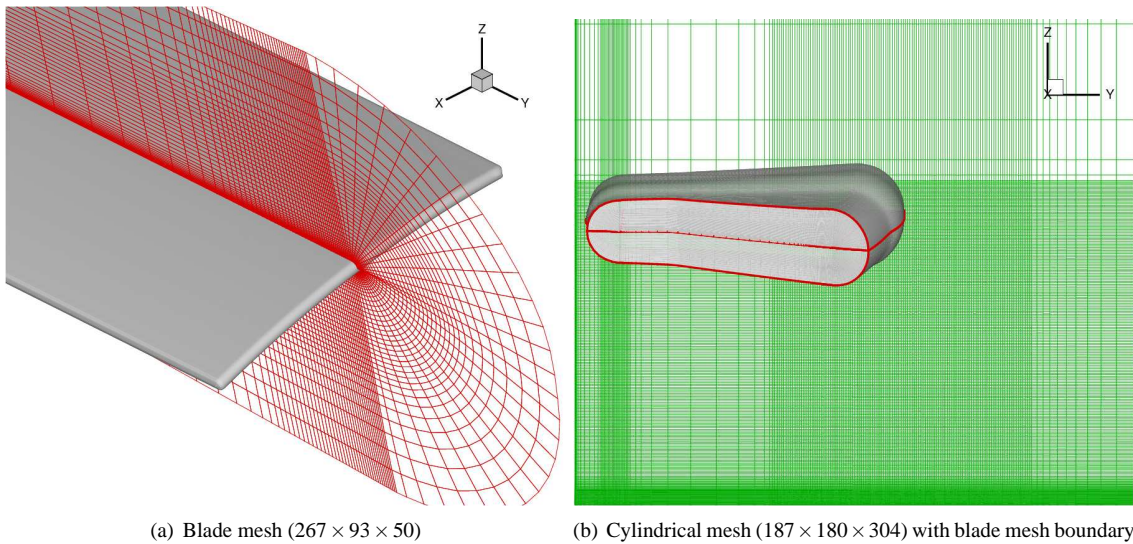


Figure 3: Mesh system used for a rotor height of  $h/R = 1.0$ .

vertical direction increases. For two cases,  $h/R = 0.25$  and  $h/R = 0.5$ , the mesh was refined to a larger radial extent to better capture the increased ground-wake interactions observed at those heights. Figure 3 shows the blade and background meshes used for the simulation of rotor height of  $1.0R$  above ground. Note that as the rotor height increases, the number of points required to capture the essential physics grows considerably. Such large problems can only be tackled with effective parallelization.

## Results

As mentioned previously, CFD calculations were performed at four different rotor heights above ground:  $h/R = 0.25, 0.5, 1R$  and  $1.5R$ . In addition, the effect of introducing a  $-10^\circ$  linear twist at  $h/R = 1.0$  was studied to understand its impact on the resulting wake IGE aerodynamics. For this case, the collective pitch was set at  $12^\circ$  to allow comparison to the untwisted blade simulations at comparable integrated rotor thrust.

### Performance at Different Rotor Heights

To gain confidence in the predictive capability of the CFD model, the predictions of the integrated thrust and power data from the calculations were compared against the measured experimental values. The spanwise distributions of the rotor thrust and power were also examined to better understand their behavior as a function of rotor height above ground, as well as the change in blade twist. The following sections describe the performance validation in greater detail.

### Integrated Performance Comparison

In OGE, the thrust ( $C_T$ ) and power coefficients ( $C_P$ ) predicted by the CFD model are 0.0143 and 0.00249, respectively, while the experimental values are 0.0133 and 0.00227, respectively. The experimental thrust and power are slightly smaller compared to the CFD values in OGE. Table 2 shows the comparison of the predicted thrust and power coefficients normalized by the OGE value along with the experimental data obtained by Lee et al. (Ref. 1) for various rotor heights above ground. From the table, it is seen that current simulation methodology accurately predicts the change in performance as rotor height above ground varies. As the rotor height above ground decreases, the thrust increases as expected, while the power remains fairly constant (marginal increase with decreasing ground distance). An exception to this trend is the predicted power for the rotor height of  $0.25R$  above ground, where the value has increased significantly. Otherwise, the overall performance change due to ground effect is well predicted by the CFD model. For the case using twisted blade at the rotor height of  $1R$  above ground, the thrust produced is very similar to the values for the

| $h/R$ | $C_T/C_{T_{OGE}}$ |       | $C_P/C_{P_{OGE}}$ |       |
|-------|-------------------|-------|-------------------|-------|
|       | Computed          | Expt. | Computed          | Expt. |
| 0.25  | 1.40              | 1.44  | 1.18              | 1.07  |
| 0.5   | 1.23              | 1.26  | 1.07              | 1.05  |
| 1.0   | 1.15              | 1.17  | 1.06              | 1.05  |
| 1.5   | 1.06              | 1.08  | 1.06              | 1.04  |

Table 2: Thrust and power comparison with experiment (Ref. 1) for different rotor heights.

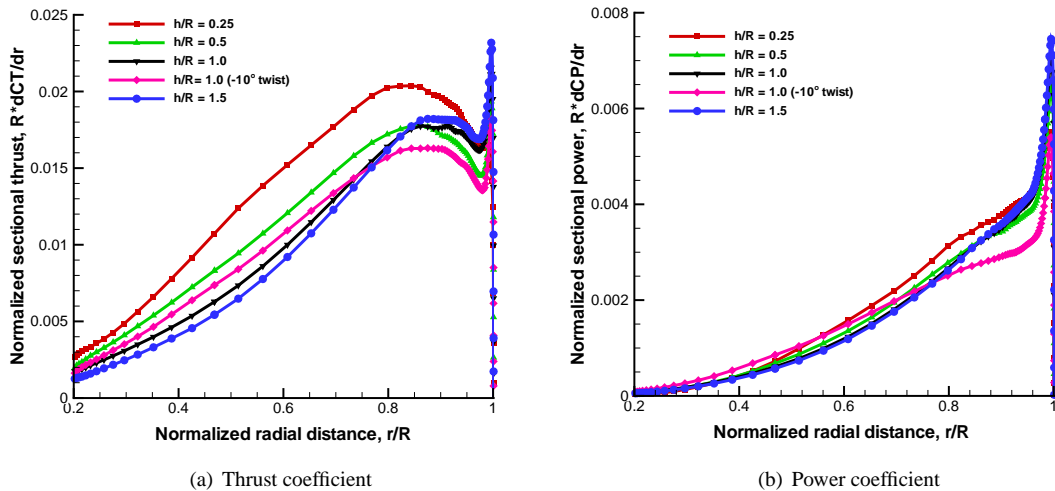


Figure 4: Spanwise thrust and power coefficients for different rotor heights.

untwisted blade at the rotor height of  $1R$  above ground, while the power is lower by about 4%. The calculated performance data shows good correlation with the measured values, and therefore, one can expect it to predict the flow-field with reasonable accuracy.

### Spanwise Performance

Spanwise distribution of  $C_T$  and  $C_P$  are plotted in Fig. 4 to understand the reason for the differences in the integrated values. From the plot, it is evident that, as the rotor height above ground decreases, the sectional thrust increases at most of the span locations. However, an opposite trend is observed near the tip region. As expected, the case that uses twisted blades produces lower thrust outboard and higher thrust inboard. Looking at the power distribution, various rotor heights above ground do not show much variation. However, using twisted blades results in significantly lower power at the outboard sections and marginally higher power at the inboard sections. Overall, the spanwise distribution looks consistent with what is expected.

### Flow-field Comparison

Following the performance validation, the current section will focus on validating the predicted flow-field with the available experimental data. PIV measurements were performed to obtain velocity fields for different ground distances. Velocities are provided at different wake-ages (phase-averaged) and also as time-averaged values.

### Phase Averaged Flow Field Comparison

Figure 5 shows the comparison of phase-averaged azimuthal vorticity contour at three different wake-ages ( $0^\circ$ ,  $60^\circ$  and  $120^\circ$ ) for the rotor height of  $1R$  above ground. The plot also shows the velocity vectors. From the plot, it can be seen that the predicted wake trajectory is very similar to that of the experiments at all wake-ages. The tip vortex is clearly resolved until it interacts with the ground. Note that the tip vortex is significantly strong even after four blade passages due to the intensification caused by stretching of the vortex filament. Comparing the magnitude of the vorticity, the experiment shows lot more dissipation compared to the computational result. The additional dissipation in the experimental data is believed to be caused because of larger tip vortex wandering observed in the experiments as compared to the CFD calculations, which causes additional vortex smearing when the velocity field is averaged over multiple revolutions.

Next, the phase-averaged azimuthal vorticity contours for the other rotor heights above ground ( $0.25R$ ,  $0.5R$  and  $1.5R$ ) are plotted in Fig. 6. Comparison with experimental data is shown at  $0^\circ$  wake-age. Overall, there is very

good agreement in the wake trajectory for all the cases, except for the rotor height of  $0.25R$  above ground. The differences in the wake trajectories for the rotor height of  $h/R = 0.25$  can be due to the presence of large instabilities in the tip vortex flow-field. More details of these instabilities will be seen in later sections.

### Time-Average Velocity Profile Comparison

A more quantitative validation can be obtained by comparing the velocity profiles for various rotor heights above ground. Figures 7, 8 and 9 show the comparison between the experimental and the computed time-averaged radial velocity profiles at four different radial locations ( $0.8R$ ,  $1R$ ,  $1.25R$  and  $1.5R$ ) for the rotor heights of  $0.25R$ ,  $0.5R$  and  $1R$  above ground, respectively. The velocities are non-dimensionalized by the ideal hover induced velocity for the corresponding thrust value. From the plot, the computations can clearly be observed to correctly predict the overall physics of the flow-field. For all the cases, the rotor induced flow is forced to expand radially outward creating a wall jet. The height of the wall jet is seen to decrease (similar to the experimental data) as one moves radially outward for all the rotor heights above ground. As a consequence, there is an increase in the peak radial velocities at larger radial distance. Comparing the predicted value of peak jet velocity with the experiments, the computed value can be observed to be higher for most of the cases. This is expected from the fact that computations predicted much stronger vortices at later wake-ages (shown earlier) and therefore, should induce stronger velocities at the ground. We can also see an improving correlation between the CFD and the experimental profiles as the rotor heights above ground increases. This is in accordance with what was seen earlier while looking at the phase-averaged azimuthal vorticity contour plots, where the predicted trajectories for the smaller rotor heights above ground showed more deviation from the experiments. Experimental data were also obtained at further outboard radial locations, where the jet becomes fully developed and the peak velocities decrease because of diffusion. In the computations, the results at these radial locations cannot be fully trusted as the calculations did not have sufficient mesh resolution to resolve the flow correctly. Therefore, the velocity profiles at these outboard positions are not plotted. It should be mentioned here that the agreement in the radial velocity profiles for the rotor height of  $1.5R$  above ground is comparable to that of the  $1R$  case.

### Phase-Averaged Velocity Profile Comparison

A more detailed validation of the calculation is performed by comparing the radial velocity profiles at different

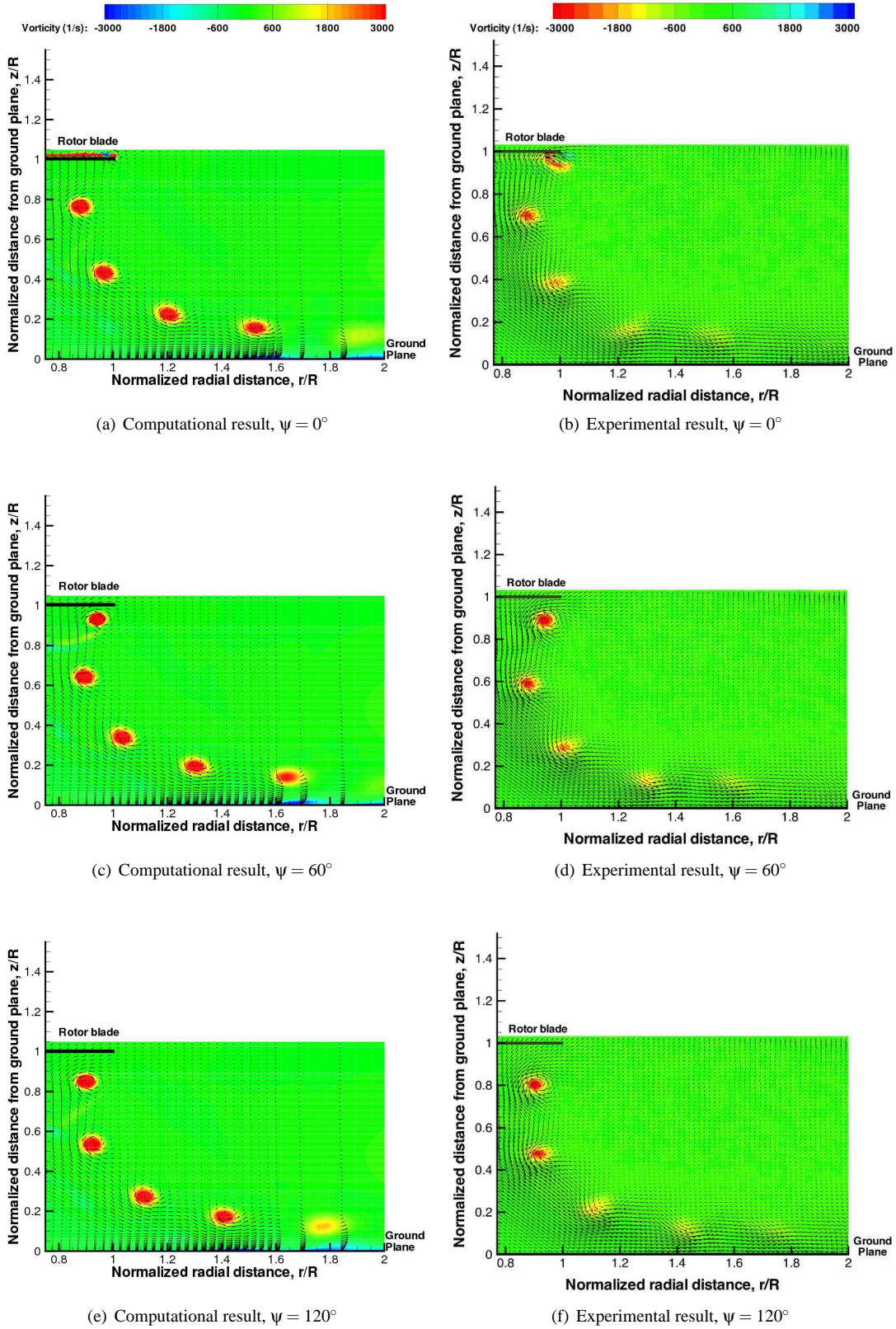
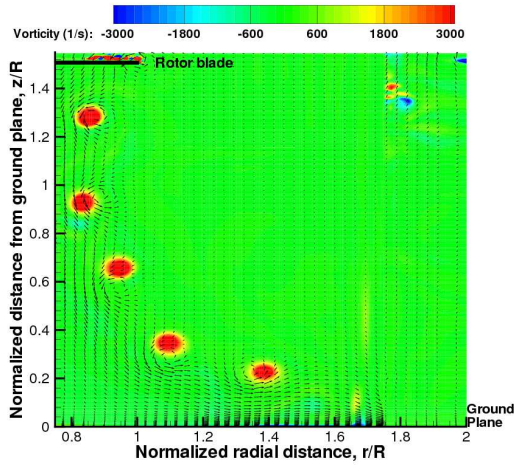
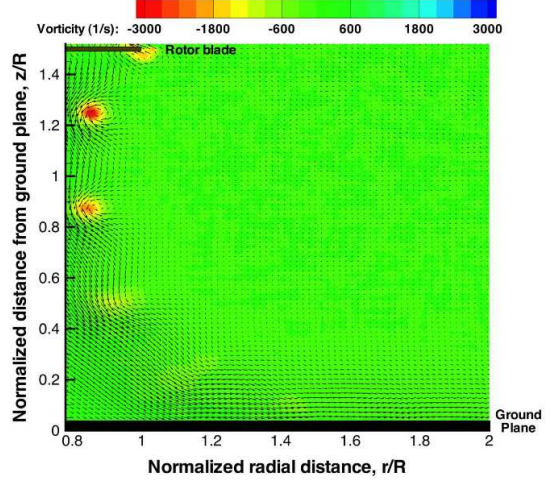


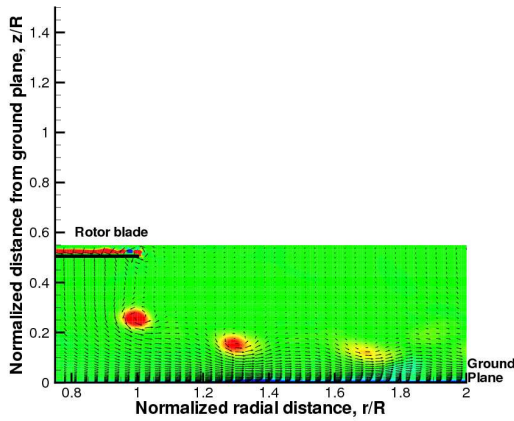
Figure 5: Comparison of CFD predicted phase-averaged vorticity contours with experimental data (Ref. 1) for a rotor height of  $h/R = 1.0$ .



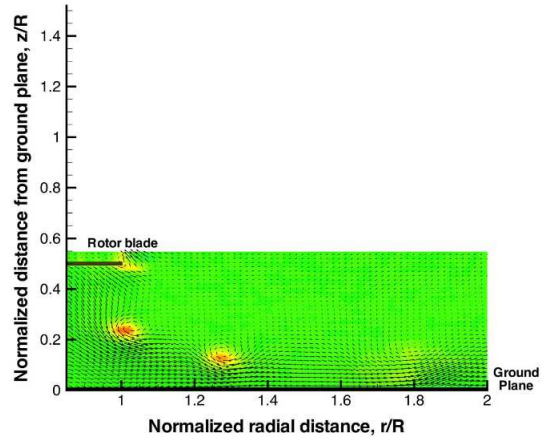
(a) Computational result,  $h/R = 1.5$



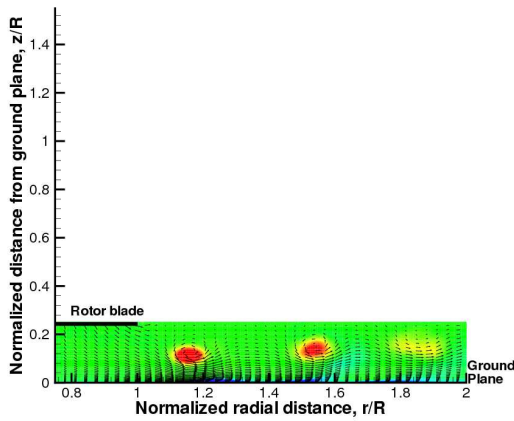
(b) Experimental result,  $h/R = 1.5$



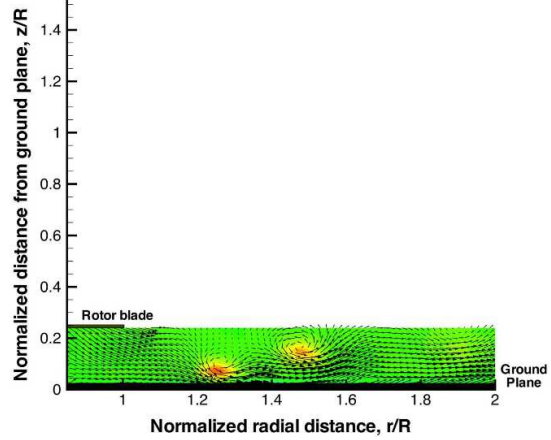
(c) Computational result,  $h/R = 0.5$



(d) Experimental result,  $h/R = 0.5$



(e) Computational result,  $h/R = 0.25$



(f) Experimental result,  $h/R = 0.25$

Figure 6: Comparison of CFD predicted phase-averaged vorticity contours with experimental data (Ref. 1) for different rotor heights,  $\psi = 0^\circ$ .

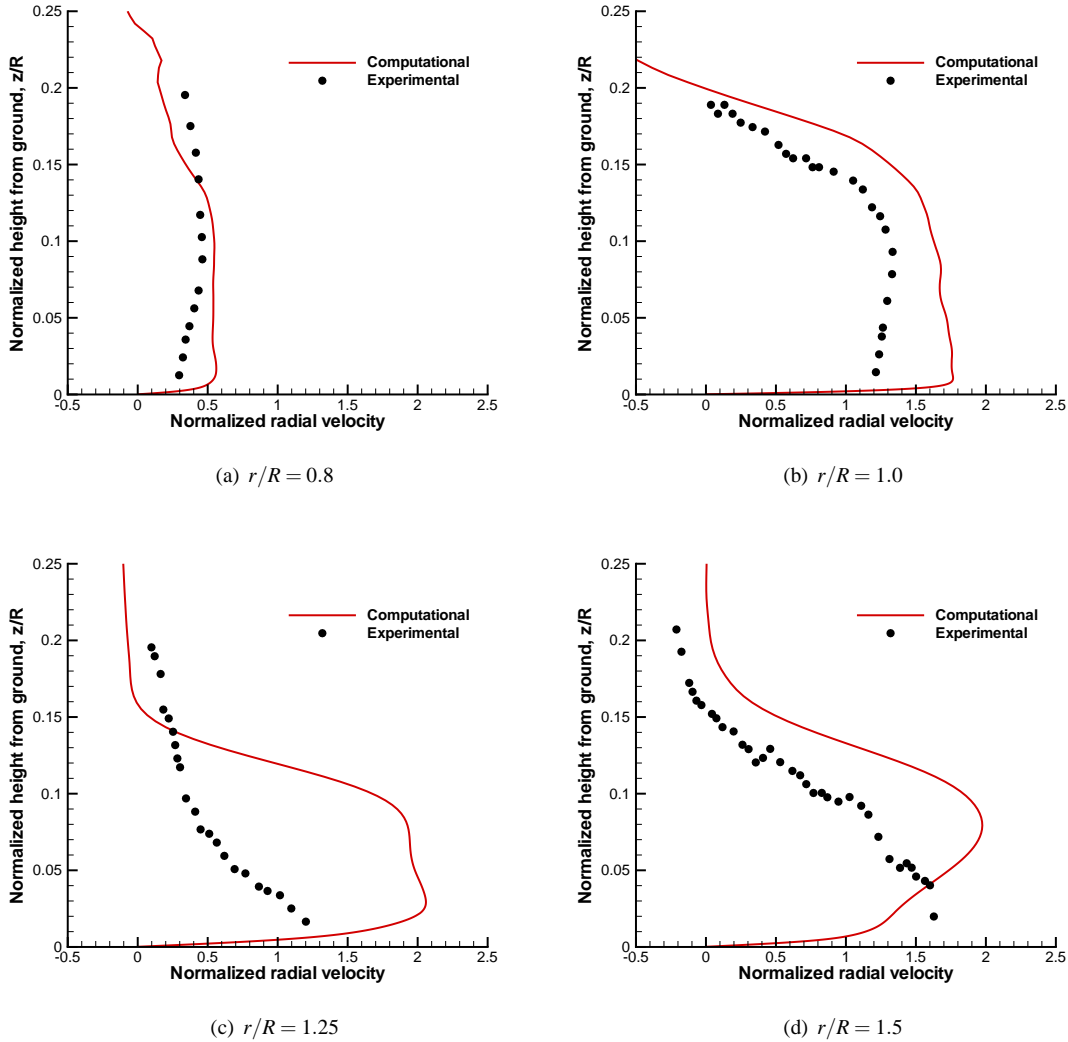


Figure 7: Comparison of CFD predicted time-averaged velocity profile with experimental data (Ref. 1) at different radial locations for a rotor height of  $h/R = 0.25$ .

wake-ages (phase-averaged) for the ground distance of  $1R$ . Figure 10 shows the comparison of radial velocity profiles (non-dimensionalized by the ideal hover induced velocity for the corresponding thrust value) at the radial locations  $0.8R$ ,  $1R$ ,  $1.25R$  and  $1.5R$ . Plotted along with this are the time-averaged radial velocity profiles, which were discussed earlier. Note that the time-averaged velocity is approximately equal to the average of all the phase-averaged velocities. The fluctuations seen in the phase-averaged radial velocity profiles are due to the local velocity induced by the presence of tip vortex. These fluctuations are indicative of the unsteadiness of the flow at the ground plane. Accurate prediction of these fluctuation is important to capture the dust entrainment correctly. Note that these fluctuations do not show up in the time-

averaged values because all the transients get averaged out. As expected, the agreement between CFD and experimental phase-averaged result is reasonable. Again, due to the stronger predicted vortex strength, the fluctuations in the computed phase-averaged velocities are larger.

### Average Inflow Velocities

Following the comparison of the radial velocities, the next logical step is to look at the inflow velocities. Figure 11 shows the radial variation of the predicted induced velocity averaged over time. The inflow is normalized by the hover induced velocity corresponding to the thrust for OGE case, so that the relative magnitudes of the inflow can be observed. The variation is shown for different ro-

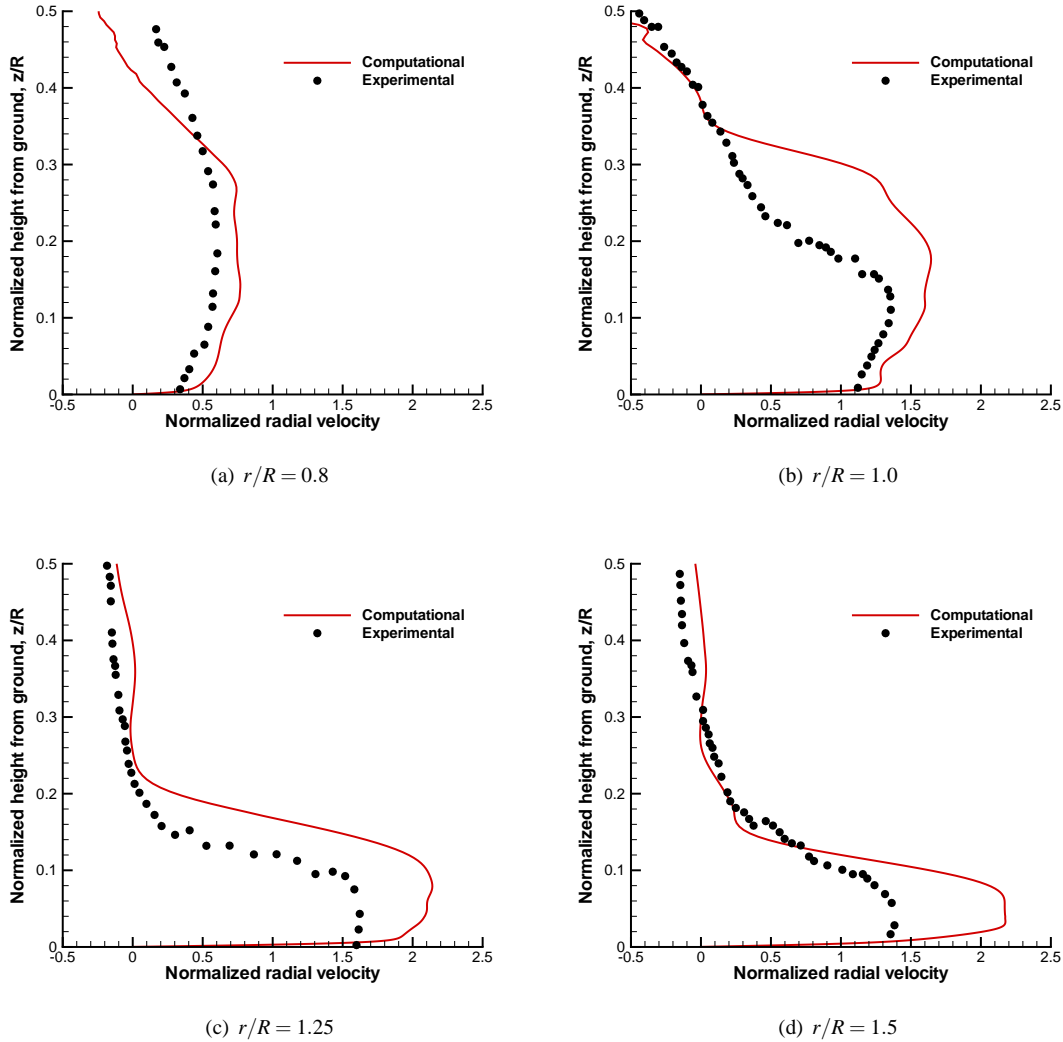


Figure 8: Comparison of CFD predicted time-averaged velocity profile with experimental data (Ref. 1) at different radial locations for a rotor height of  $h/R = 0.5$ .

tor heights of  $1R$ ,  $1R$  using twisted blade,  $0.5R$  and  $0.25R$  above ground. For each case, the variation is plotted at four different planes above ground. Three of the planes correspond to one-fourth, one-half and three-fourths the distance from the ground to the plane of rotor. The fourth one is at the plane of the rotor given by  $z/R = h/R$  for any particular rotor height above ground,  $h/R$ . In order to minimize the influence of the rotor blade, the inflow at the plane of the rotor was obtained by averaging values for the plane  $0.1$  chords above and below the rotor plane.

All the important characteristics of the rotor wake are captured in these plots. The wake boundaries can be clearly seen in all the plots. For the rotor height of  $1R$  above ground, the wake is observed to contract initially, which then expands as it gets closer to the ground. For the

rotor height of  $1R$  above ground that uses twisted blades, the wake contracts initially but then starts to expand at an earlier wake age. The reason for the differences in the wake contraction between the twisted and the untwisted blade cases is possibly because of the higher inflow in-board with the use of twisted blades, which makes the wake turn faster. For the  $h/R = 0.5$  case, the wake starts expanding almost from the initial wake-ages in order to adjust for the ground. The unsteadiness developing near the ground is clearly evident. The unsteadiness gets more prominent for the  $h/R = 0.25$  case, where the wake expands even faster. As expected, the peak inflow in all the plots increases or decreases based on whether the wake contracts or expands.

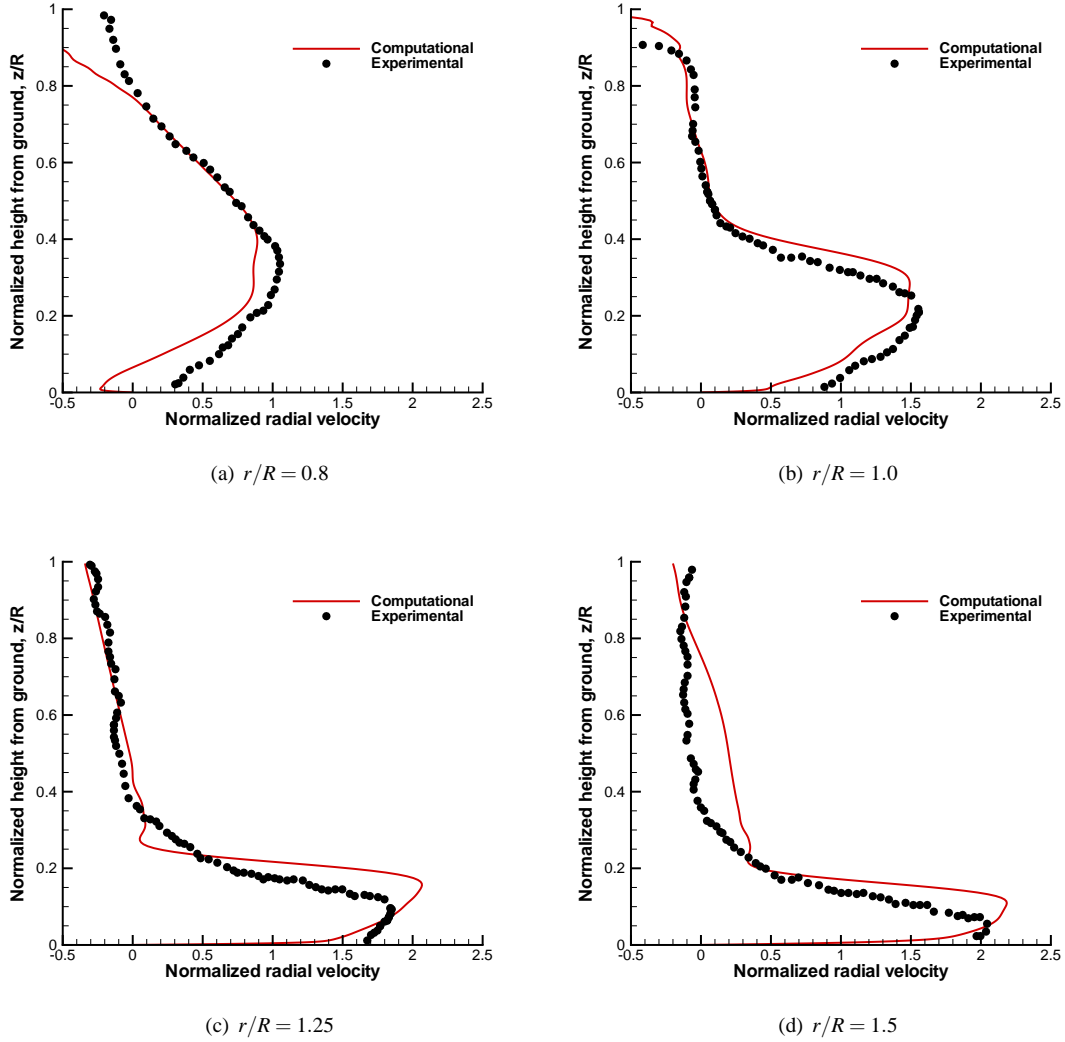


Figure 9: Comparison of CFD predicted time-averaged velocity profile with experimental data (Ref. 1) at different radial locations for a rotor height of  $h/R = 1.0$ .

## Flow-field Visualizations

Iso-surfaces of  $q$ -criterion (Ref. 18) can be used to better view the tip vortex flow-field for various rotor heights above ground cases. Figure 12 shows the iso-surfaces of  $q$ -criterion,  $q = 0.25$  colored with azimuthal vorticity contour for the rotor heights off the ground, namely  $h/R = 1.0, 1.0$  with  $-10^\circ$  blade twist,  $0.5$  and  $0.25$ . Though the simulations are only performed for half the actual domain with the assumption of periodicity, the solution for the entire domain is plotted for better viewing. From the plots, it is evident that the instabilities in the vortices increase as the rotor height above ground decreases. There are several reasons that cause the development of these instabilities. First, the thrust produced by the blade at

smaller rotor heights above ground is larger. Therefore, not only is the strength of the tip vortex larger, which leads to increased vortex-vortex interactions, but there is also increased separation near the tip of the blade, which seeds the instability. Second, the strength of tip vortex is further intensified due to the rapid expansion of the wake at smaller rotor heights above ground, which further increases the vortex-vortex interactions. In addition, an increased interaction of these strong vortices with the ground acts as an additional destabilization factor. At the rotor heights of  $0.25R$  and  $0.5R$  above ground, additional flow structures are formed near the ground. It will become evident later that these are formed due to flow separation at the ground. Due to the extremely complicated flow-field found at smaller rotor heights above ground, it

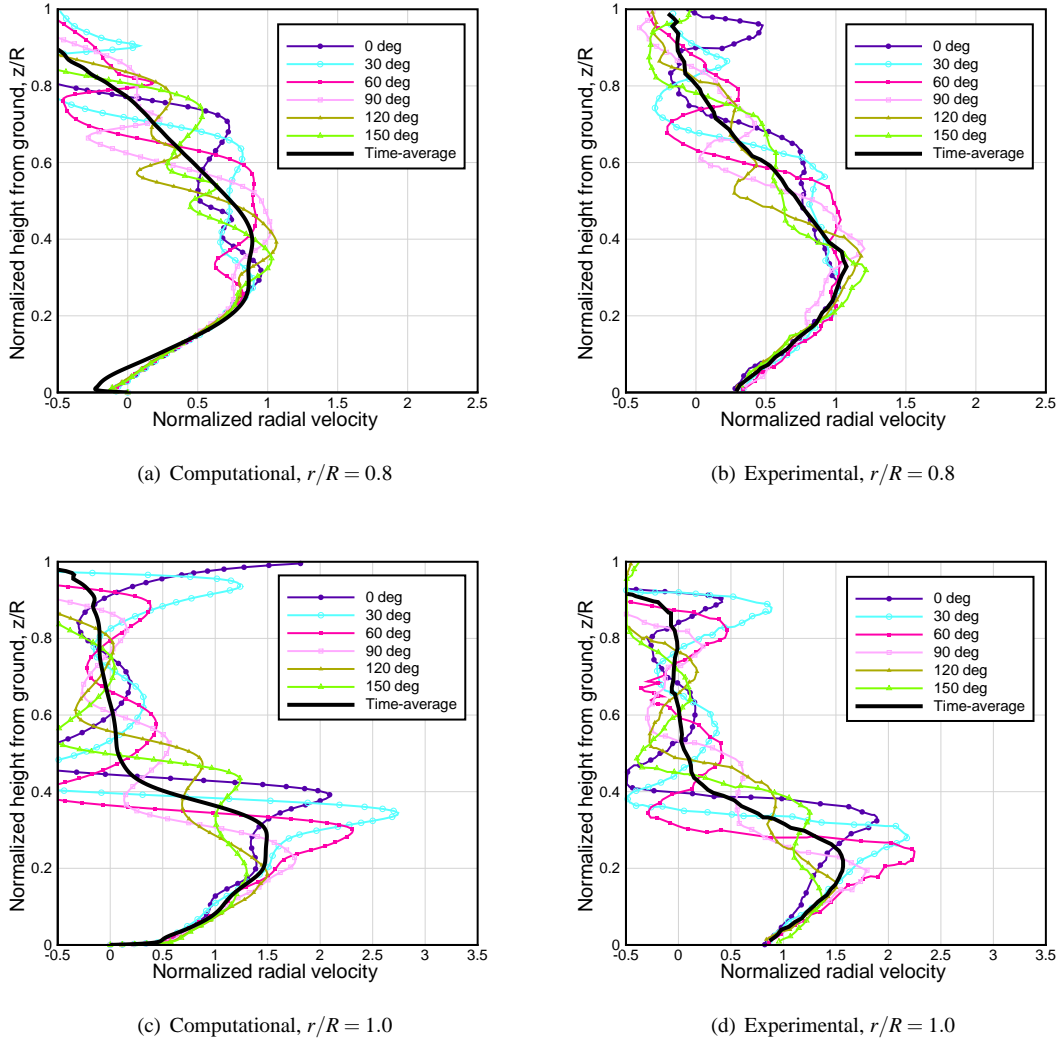


Figure 10: Comparison of CFD predicted phase-averaged velocity profiles with experimental data (Ref. 1) at various radial locations for a rotor height of  $h/R = 1.0$ . (con'td...)

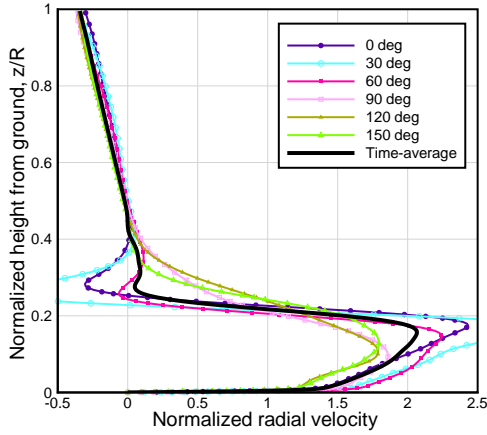
becomes very challenging to accurately predict the velocity fields at these distances, especially for the rotor height of  $0.25R$  above the ground (seen earlier).

Comparing the vortex trajectories for the twisted and untwisted blade at rotor height of  $1R$  above ground, it can be seen that the case with the blade twist has additional instabilities in the wake. The primary reason for this is because the twisted blade configuration has a more uniform inflow, which results in a decrease in downwash towards the tip of the blade. As a result, the tip vortex convects down at slower rate, thus resulting in increased vortex-vortex interactions. Note that the strength of the tip vortex emanating from the blade is not too different for both the cases, as the thrust for both are almost comparable. However, the tip vortex for the case with

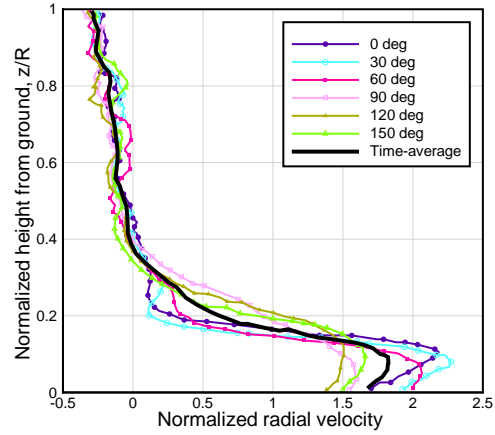
blade twist gets intensified marginally faster because of a slightly faster wake expansion rate during the initial wake-ages. This acts as a secondary reason for increased vortex-vortex interactions, thereby amplifying the instabilities.

### Velocities at the Ground

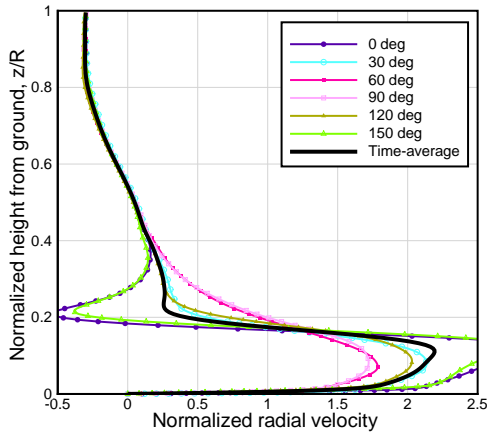
Due to relatively thin boundary layer region (less than 5% of rotor radius), the experiments did not explore in much detail the nature of boundary layer. When the boundary layer is thin, PIV requires very fine spatial resolution near the ground and must minimize laser reflections, both of which pose extreme challenges. Therefore, there is no experimental validation for the velocities predicted by cur-



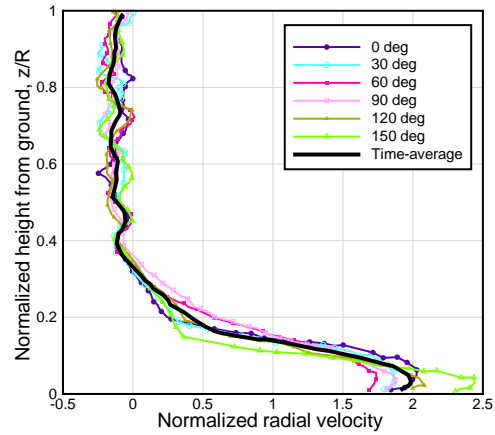
(e) Computational,  $r/R = 1.25$



(f) Experimental,  $r/R = 1.25$



(g) Computational,  $r/R = 1.5$



(h) Experimental,  $r/R = 1.5$

Figure 10: Comparison of CFD predicted phase-averaged velocity profiles with experimental data (Ref. 1) at various radial locations for a rotor height of  $h/R = 1.0$ .

rent simulation methodology near the ground. However, the current CFD solution can still be used to explore some of the physics near the ground.

Figures 13, 14, 15, and 16 show the velocity vectors along with the pressure contours (normalized by freestream value) for the rotor heights of  $1R$ ,  $1R$  with  $-10^\circ$  blade twist,  $0.5R$  and  $0.25R$  above ground respectively. For the purpose of clarity, the vectors are plotted only one in every six points in the normal direction and one in every three points in the radial direction from the mesh used for simulation. In all the cases, the tip vortex can be easily identified by the low pressure region. For the rotor height of  $1R$  above ground, the flow-field does not appear very complicated. There is a region of high pressure on the ground corresponding to the stagna-

tion location. The jet flow at the ground is directed outwards at locations outboard of the stagnation point and inwards inboard of it. The boundary layer developed near the ground is mostly laminar, which becomes more turbulent at regions directly below tip vortex as a result of additional local induced velocity. There could be an increased entrainment of particles from these regions of the ground. For the rotor height of  $1R$  with  $-10^\circ$  blade twist above ground, the instabilities developed in the wake can be very clearly seen in Fig. 14, by identifying that the position of the tip vortex does not change smoothly from one wake-age to the other. The instabilities seems to have induced flow separation at around  $r/R = 1.25$  at  $60^\circ$  wake-age.

Looking at the plots for smaller rotor heights of  $0.25R$

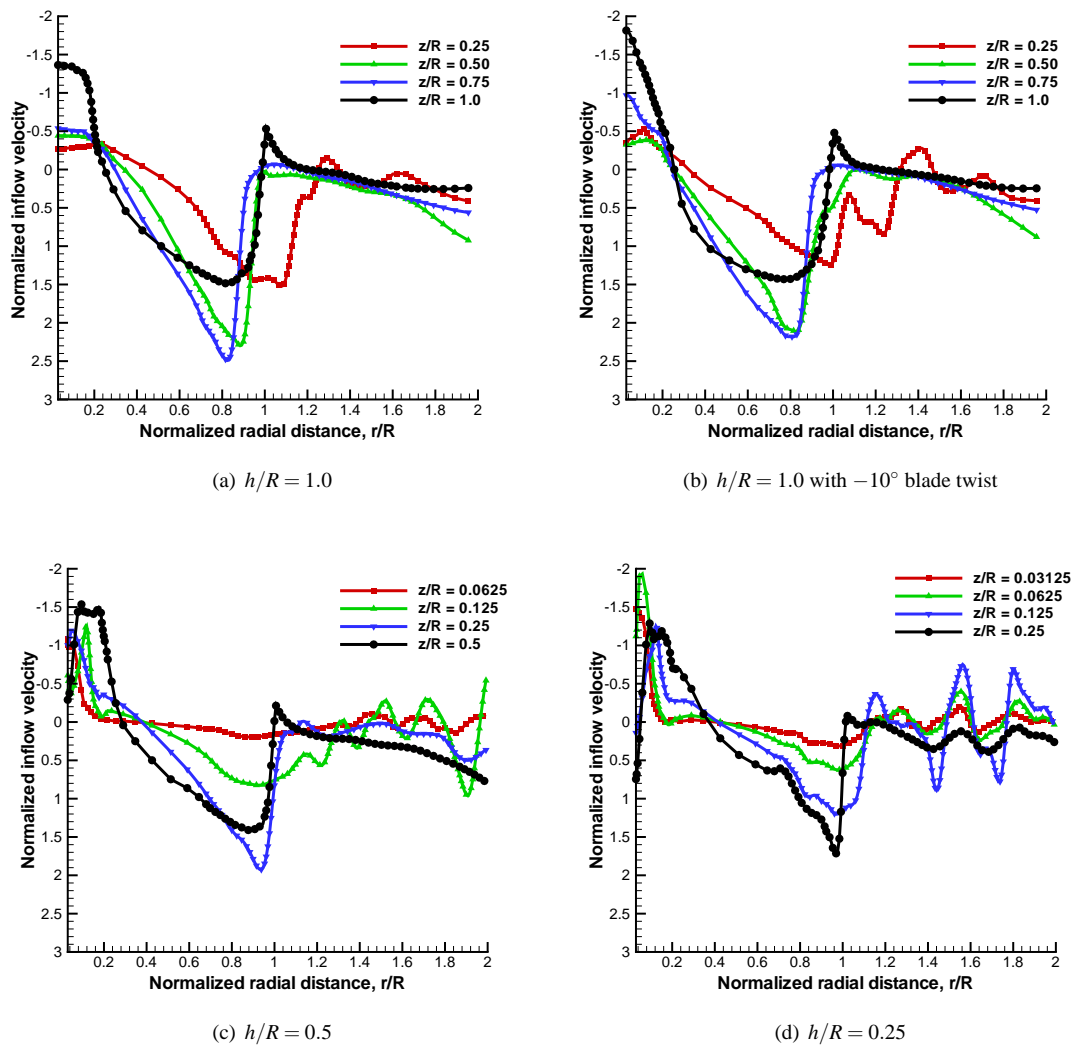


Figure 11: Inflow velocity at different planes below the rotor for various rotor heights above ground.

and  $0.5R$  above ground (Figs. 15 and 16, respectively), it can be seen that there is an increased interaction of the tip vortex with the ground as the rotor height above ground decreases. For these cases, the tip vortex is observed to come much closer to the ground compared to the  $1R$  case. As a result, the flow separates at the location on the ground that is directly below the vortex. The separated flow then reattaches at an outboard location on the ground where the influence of the tip vortex is lower, thus forming a separation bubble. The region of separation bubble is also marked by low pressure. The separation bubble formed at one wake-age is observed to detach from the ground at a later wake-age forming a small opposite sign vortex. The opposite sign vortex interacts with the tip vortex, thereby further developing instabilities. The strength of this opposite sign vortex is larger

for smaller rotor heights above ground. Another interesting feature to notice for the smaller rotor heights ( $0.5R$  and  $0.25R$ ) above ground is the large high pressure region produced by the blade directly below the rotor at  $0^\circ$  wake-age. Such large pressure can accelerate the jet flow near the ground.

### Eddy Viscosity Contours

Eddy viscosity contours can be used to better view the turbulence levels at the ground. Figures 17, 18 and 19 show the eddy viscosity contours (normalized by laminar viscosity) for the rotor heights of  $1.0R$ ,  $0.5R$  and  $0.25R$  above ground respectively, at two different representative planes. The first plane is cut parallel to the ground at a height of  $0.03R$  above ground. The second plane is shown

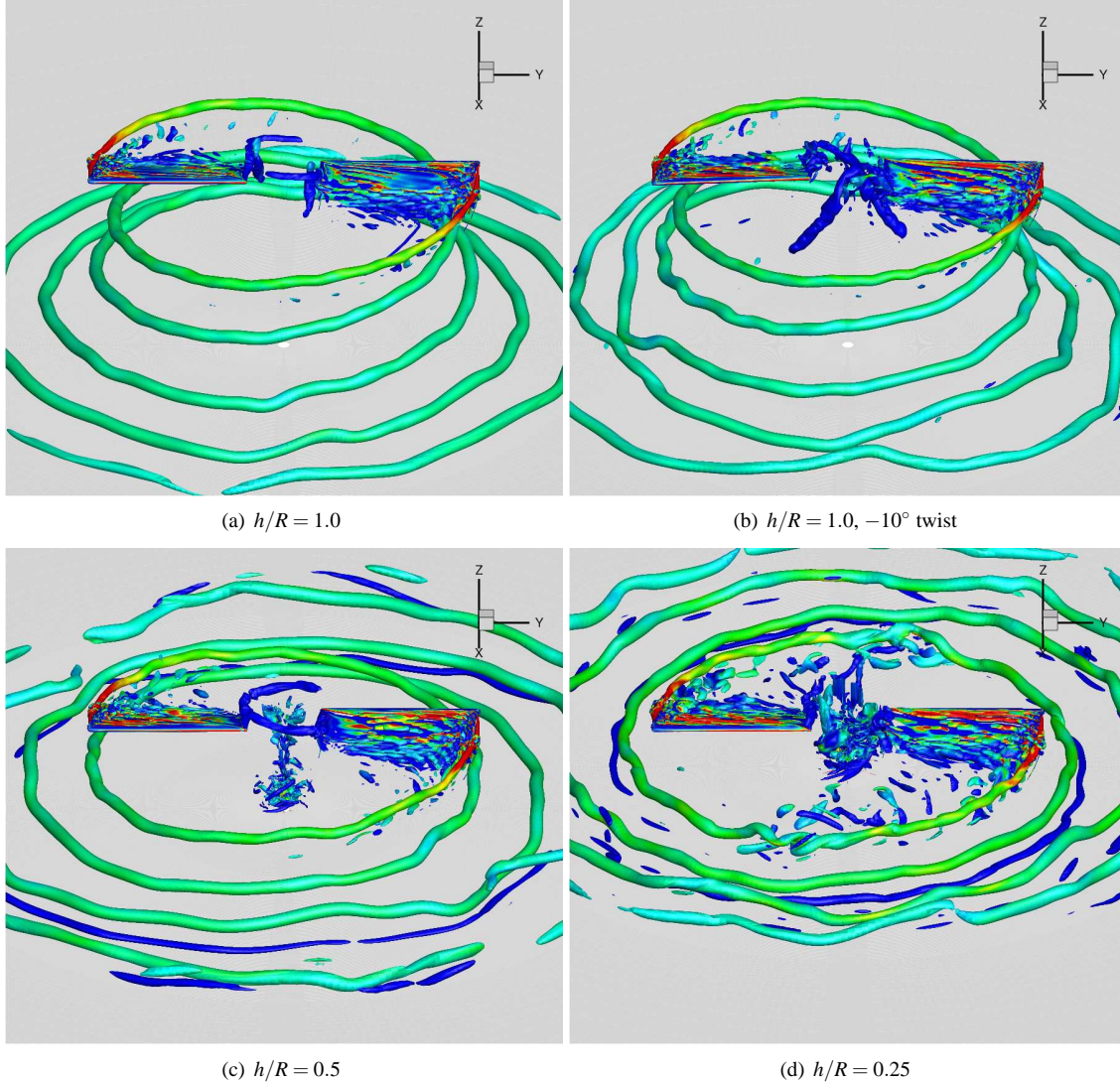


Figure 12: Iso-surfaces of  $q$ -criterion,  $q = 0.25$  for different rotor heights above ground.

at  $60^\circ$  wake-age. From the plots, it is seen that the overall magnitude of eddy viscosity is very low for all the cases. In fact, the values of eddy viscosity is less than the laminar viscosity at most of the regions, suggesting that most of the flow on the ground is nearly laminar. The experimental flow visualization showed more turbulence in the flow-field, see Fig. 2(b). One of the possible reasons for the differences could be due to the additional turbulence introduced by the mounting apparatus in the experiments, which is not modeled in the computations.

Comparing the eddy viscosity contours for various rotor heights above ground, it is seen that the magnitude of eddy viscosity increases as the rotor height above ground decreases. For all the rotor heights above ground, there is a region of higher eddy viscosity formed directly below the vortex, which corresponds to the turbulent boundary

layer region observed in the velocity vector plots. However, at lower rotor heights above ground, the higher eddy viscosity region from the vortex (eddy viscosity gets fed into the vortex from the inboard sheet) interacts with the higher eddy viscosity region formed near the ground, resulting in an intermixing of the turbulence levels.

## Summary and Conclusions

A compressible Reynolds Averaged Navier Stokes (RANS) solver was used to simulate a hovering micro-rotor operating at very low tip Reynolds number in ground effect, with the primary objective of demonstrating its capability to provide good flow-field predictions for a hovering rotor operating close to the ground. The

computations were validated with experimentally measured mean thrust and power. This was then followed by a detailed validation of the tip vortex flow-field with the experimental PIV data. In addition, the CFD data was used to explore the details of ground-wake interactions at various rotor heights. Further, studies were performed to understand the effect of using twisted blade on the flow-field at one particular rotor height above ground. The following are specific conclusions that can be drawn from the present work :

1. The computations of rotor thrust and power coefficients showed good comparison with the available experimental data. With decreasing rotor height above ground, the thrust increased at a fairly constant power. The spanwise distribution of thrust and power followed the expected trend.
2. The phase averaged azimuthal vorticity contours for different wake ages showed good comparison with the experimental results in terms of wake trajectory. However, the predicted strength of the vortex, especially at later wake-ages, was larger compared to the experimental values. The discrepancy can be attributed to the fact that no corrections to account for the vortex wandering were applied during the process of obtaining phase-averaged velocity fields from PIV measurements over multiple rotor revolutions. This results in additional smearing of the rotor tip-vortices in the measurements.
3. The comparison of predicted time-averaged radial velocity profiles with the experimental data at different radial locations for various ground distances showed improving correlation as the rotor height above ground increased. The comparison of velocities averaged at different wake-ages reflected the fact that the predicted strength of tip vortex is larger at later wake-ages. However, the comparison was still very reasonable.
4. Flow visualization with the aid of  $q$ -criterion showed qualitative estimation of the amount of unsteadiness in the flow field. Unsteadiness increased with a decrease in the rotor height above ground.
5. Velocity vectors near the ground show that the boundary layer is nearly laminar at most of the regions. At locations on the ground directly below the vortex, the local induced velocity of the tip vortex transitions the boundary layer to a more turbulent layer.
6. The interaction of the tip vortex with the ground was observed to increase as the rotor height above ground decreases. At lower rotor heights above

ground, the increased induced velocity from the tip vortex causes the jet flow on the ground to separate and form a separation bubble. The separation bubble formed at one wake-age is seen to peel off at a later wake-age forming an opposite sign vortex. The opposite sign vortex was observed to further interact with the tip vortex.

7. Looking at the eddy viscosity further confirmed that most of the region near the ground is nearly laminar. An increase in eddy viscosity was seen at locations on the ground directly below the ground. At lower rotor heights above ground, there were evidence of eddy viscosity from the tip vortex intermixing with the eddy viscosity generated at the ground.
8. A twisted blade was seen to generate a higher degree of unsteadiness in the flow-field; this can be attributed to increased vortex-vortex interactions.

As a concluding remark, the current paper demonstrates the capability of using a wake capturing method to understand the physics of a hovering micro-rotor operating near ground. Future work will focus on a more detailed validation of the velocity fields very close to the ground, when the experimental data become available. In addition, detailed PIV measurements are being performed at the University of Maryland on a sub-scale rotor (1 m radius) operating near ground. The current solver will be further validated against these experimental results.

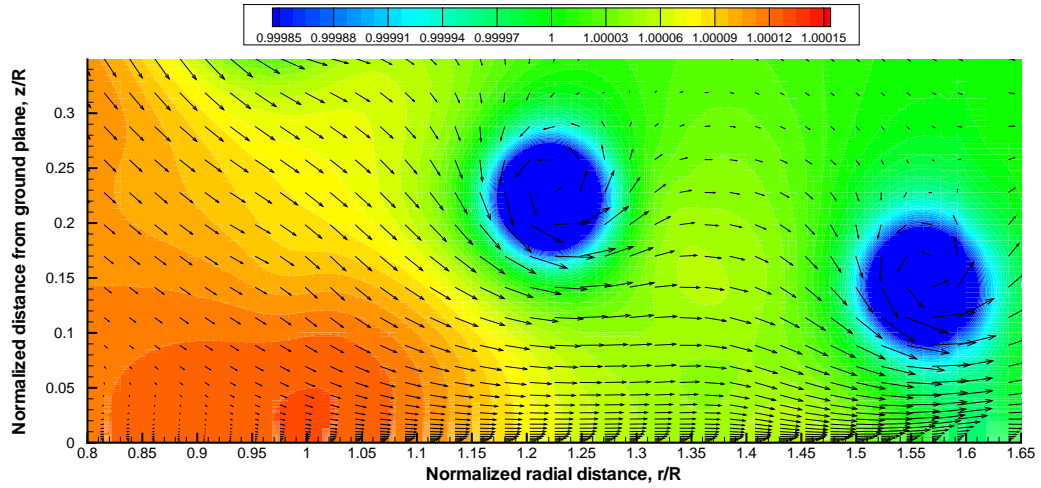
## Acknowledgments

The Air Force Office of Scientific Research supported this work under a Multidisciplinary University Research Initiative, Grant W911NF0410176. The contract monitor was Dr. Douglas Smith. The authors wish to thank all of their colleagues at the University of Maryland, Government research labs, and the rotorcraft industry for the valuable discussions on the brownout problem.

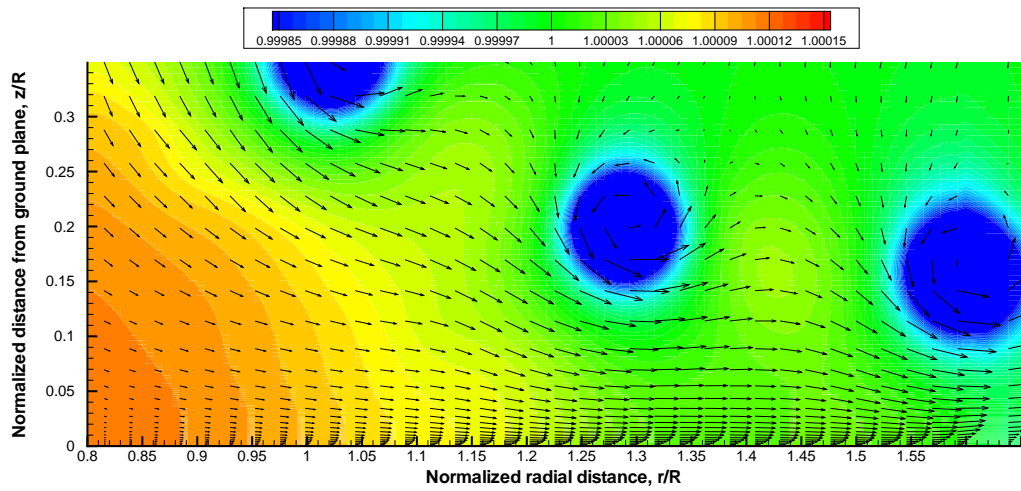
## References

- <sup>1</sup>Lee, T. E., Leishman, J. G., and Ramasamy, M., "Fluid Dynamics of Interacting Blade Tip Vortices With a Ground Plane," American Helicopter Society 64th Annual Forum Proceedings, Montr'eal, Canada, April 29–May 1, 2008.
- <sup>2</sup>Johnson, B., Leishman, J. G., and Sydney, A., "Investigation of Sediment Entrainment in Brownout Using High-Speed Particle Image Velocimetry," American Helicopter Society 65th Annual Forum Proceedings, , Grapevine, TX, May 27–29, 2009.

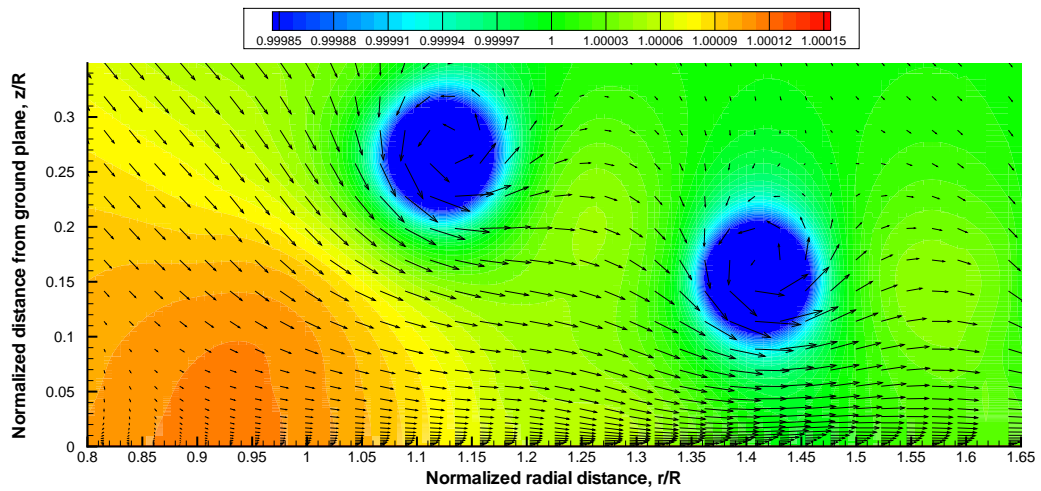
- <sup>3</sup>Nathan, N.D., and Green, R.B., “Measurements of a rotor flow in ground effect and visualization of the brownout phenomenon,” American Helicopter Society 64th Annual Forum Proceedings, Montr’éal, Canada, April 29–May 1, 2008.
- <sup>4</sup>Wachspress, D.A., Whitehouse, G.R., Keller, J.D., , Yu, K., Gilmore, P., Dorsett, M., McClure, K., “High Fidelity Rotor Aerodynamic Module for Real Time Rotorcraft Flight Simulation,” American Helicopter Society 65th Annual Forum Proceedings, Grapevine, TX, May 27–29, 2009.
- <sup>5</sup>Syal, M., and Leishman, J.G., “Efficient Mesoscale Sediment Tracking Methodology to Analyze Brownout Cloud Development,” American Helicopter Society 66th Annual Forum Proceedings, Phoenix, Az, May 11–13, 2010.
- <sup>6</sup>Phillips, C., and Brown, R.E., “Eulerian Simulation of the Fluid Dynamics of Helicopter Brownout,” American Helicopter Society 64th Annual Forum Proceedings, Montr’éal, Canada, April 29–May 1, 2008.
- <sup>7</sup>Wenren, Y., Fan, M., Wang, L. and Steinhoff, J., “Vorticity Confinement and Advanced Rendering to Compute and Visualize Complex Flows,” AIAA Paper 2006-945, 44th AIAA Aerospace Sciences Meeting and Exhibit, Reno, NV, January 9–12, 2006.
- <sup>8</sup>Lakshminarayan, V. K., and Baeder, J. D., “Computational Investigation of Micro Hovering Rotor Aerodynamics,” *Journal of the American Helicopter Society*, Vol. 55, (2), April, 2010.
- <sup>9</sup>Lakshminarayan, V. K., “Computational Investigation of Micro-Scale Coaxial Rotor Aerodynamics in Hover,” Ph.D. dissertation, Department of Aerospace Engineering, University of Maryland at College Park, 2009.
- <sup>10</sup>Koren, B., Upwind Schemes, “Multigrid and Defect Correction for the Steady Navier-Stokes Equations”, Proceedings of the 11th International Conference on Numerical Methods in Fluid Dynamics , Williamsburg, VA, June 1988.
- <sup>11</sup>Buelow P. E. O., Schwer D. A., Feng J., and Merkle C. L. “A Preconditioned Dual-Time, Diagonalized ADI scheme for Unsteady Computations,” AIAA paper 1997-2101, 13th AIAA Computational Fluid Dynamics Conference, Snowmass Village, CO, June 29–July 2, 1997.
- <sup>12</sup>Pandya, S. A., Venkateswaran, S., and Pulliam, T. H. “Implementation of Preconditioned Dual-Time Procedures in OVERFLOW,” AIAA paper 2003-0072, 41st AIAA Aerospace Sciences Meeting and Exhibit, Reno, NV, January 6–9, 2003.
- <sup>13</sup>Pulliam, T., and Chaussee, D., “A Diagonal Form of an Implicit Approximate Factorization Algorithm,” *Journal of Computational Physics*, Vol. 39, (2), February 1981, pp. 347–363.
- <sup>14</sup>Turkel, E., “Preconditioning Techniques in Computational Fluid Dynamics,” *Annual Review of Fluid Mechanics*, Vol. 31, January 1999, pp. 385–416.
- <sup>15</sup>Spalart, P. R., and Allmaras, S. R., “A One-equation Turbulence Model for Aerodynamic Flows,” AIAA Paper 1992-0439, 30th AIAA Aerospace Sciences Meeting and Exhibit, Reno, NV, January 6–9, 1992.
- <sup>16</sup>Duraisamy, K., “Studies in Tip Vortex Formation, Evolution and Control,” Ph.D. Dissertation, Department of Aerospace Engineering, University of Maryland at College Park, 2005.
- <sup>17</sup>Lee, Y., “On Overset Grids Connectivity and Automated Vortex Tracking in Rotorcraft CFD,” Ph.D. Dissertation, Department of Aerospace Engineering, University of Maryland at College Park, 2008.
- <sup>18</sup>Jeong, J., and Hussain, F., “On the Identification of a Vortex,” *Journal of Fluid Mechanics*, Vol. 285, 1995, pp. 69–94.



(a)  $\psi = 0^\circ$

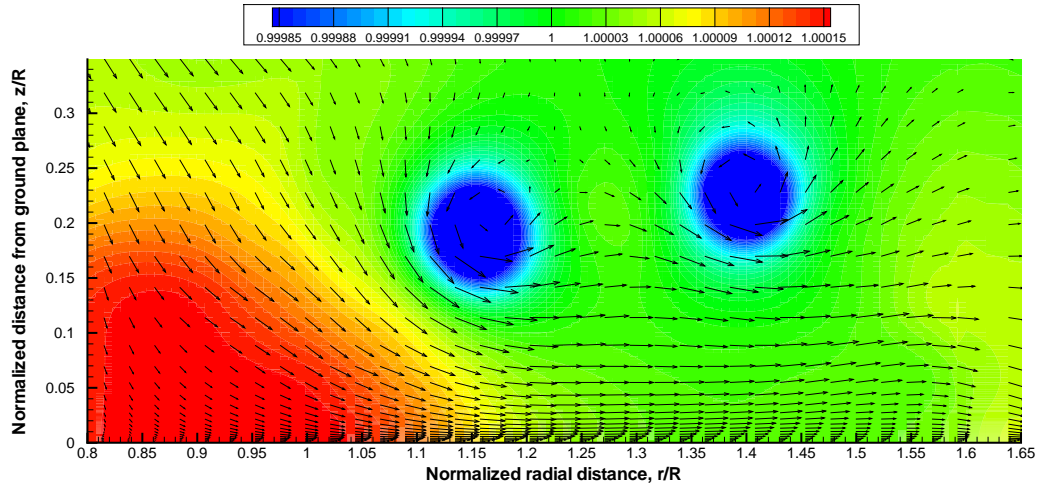


(b)  $\psi = 60^\circ$

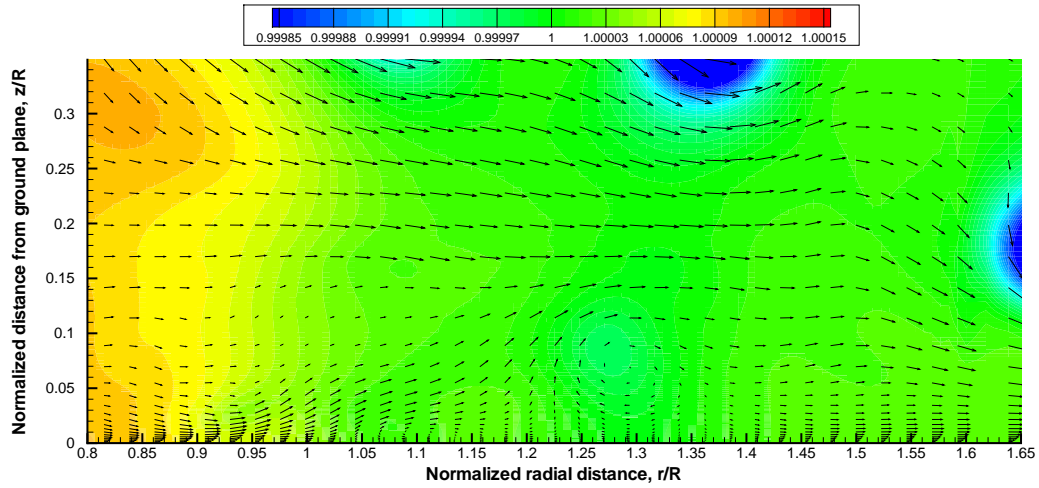


(c)  $\psi = 120^\circ$

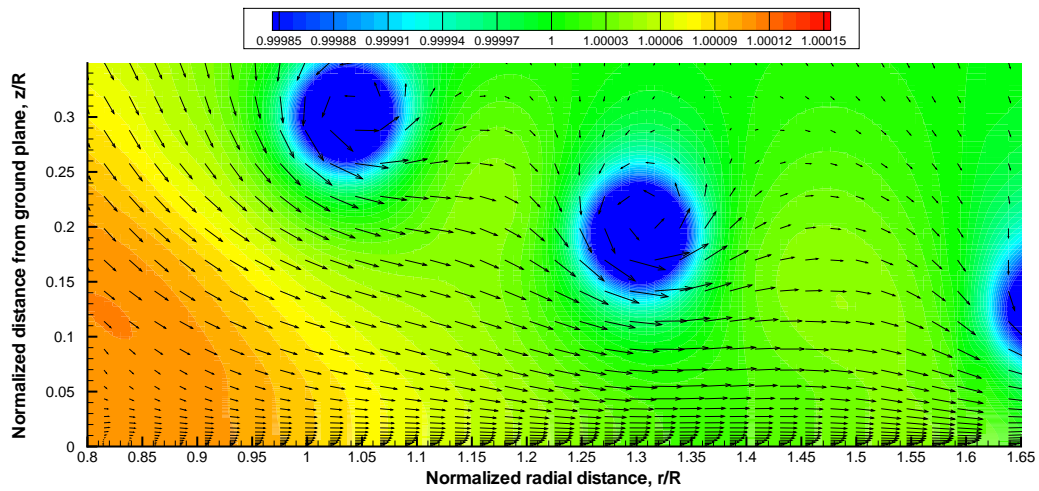
Figure 13: Velocity vectors along with pressure (non-dimensionalized by freestream value) contours for a rotor height of  $h/R = 1.0$ .



(a)  $\psi = 0^\circ$

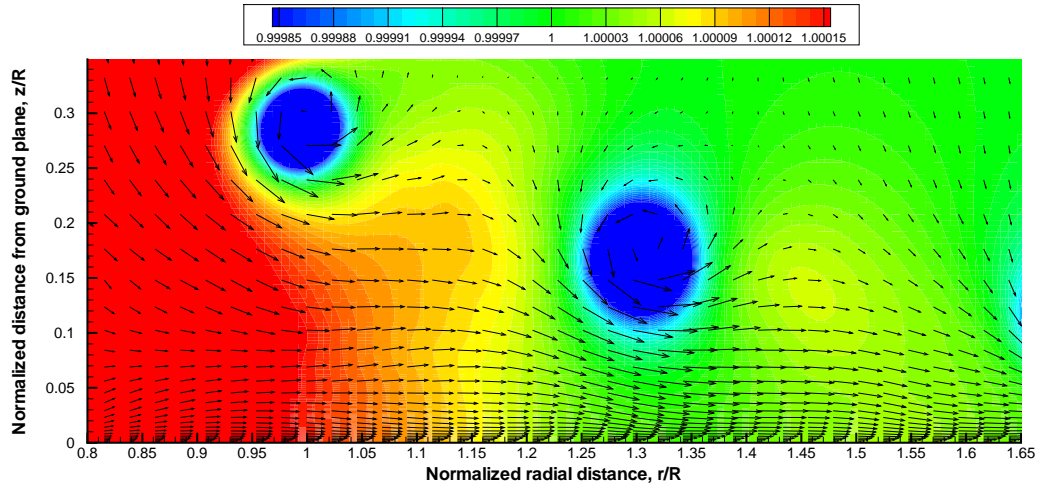


(b)  $\psi = 60^\circ$

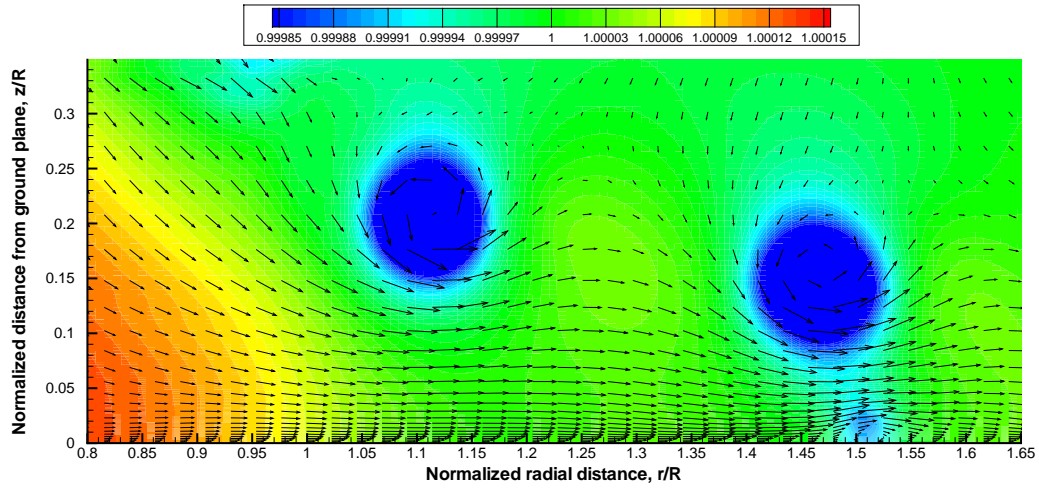


(c)  $\psi = 120^\circ$

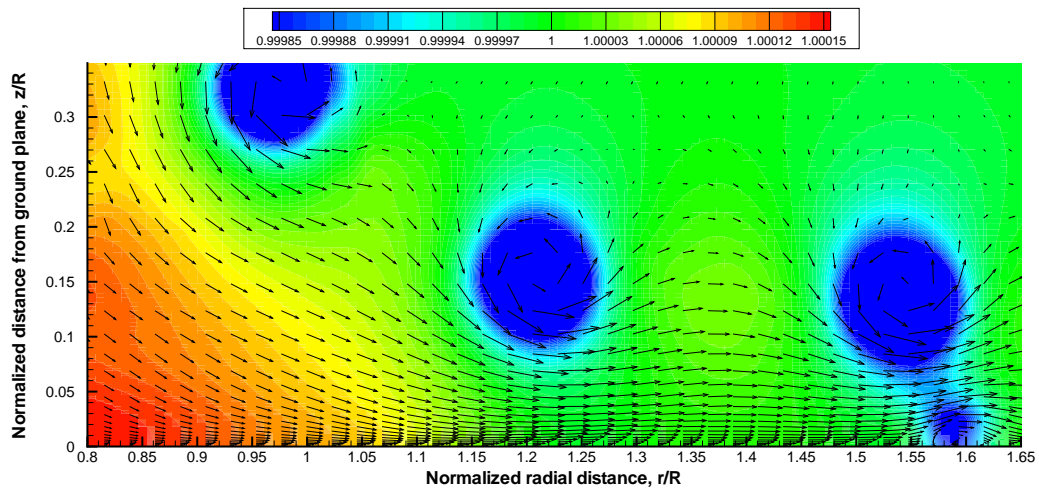
Figure 14: Velocity vectors along with pressure (non-dimensionalized by freestream value) contours for a rotor height of  $h/R = 1.0$  with  $-10^\circ$  blade twist.



(a)  $\psi = 0^\circ$

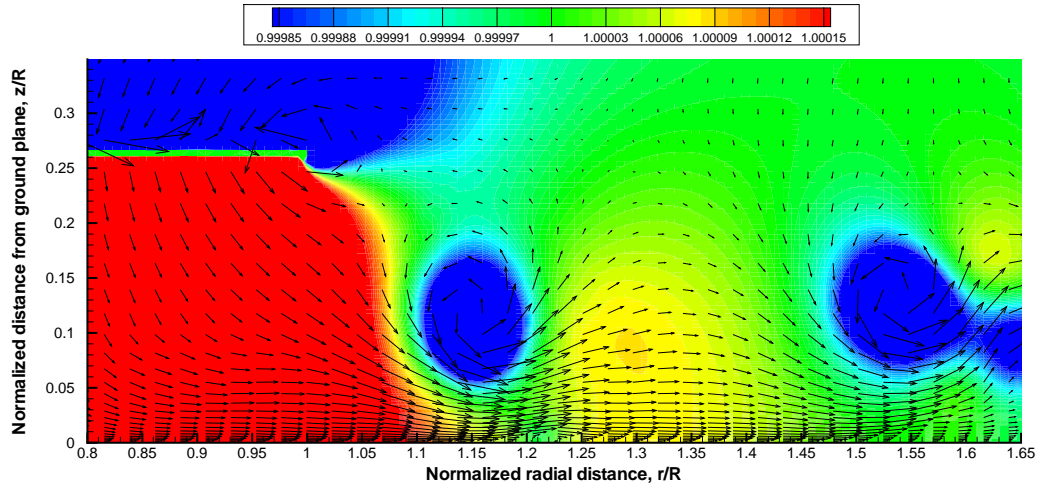


(b)  $\psi = 60^\circ$

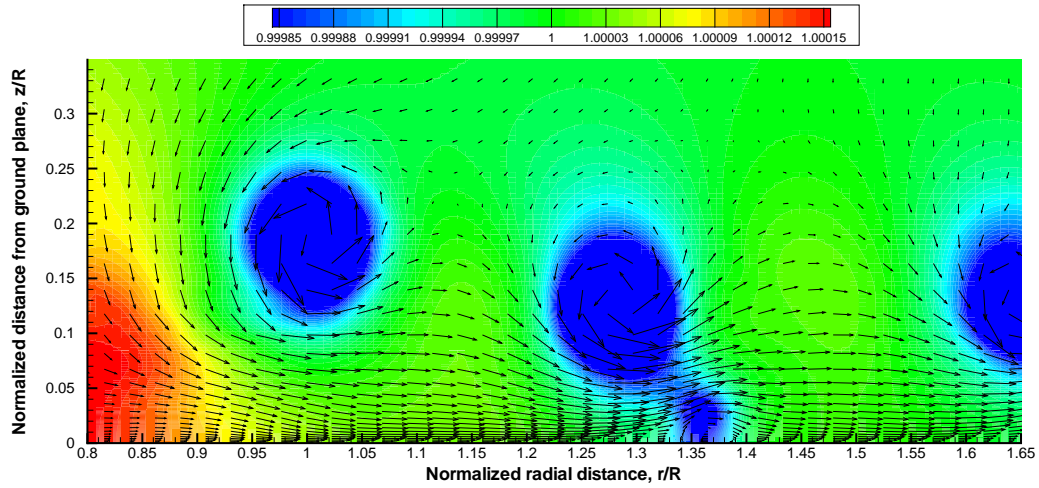


(c)  $\psi = 120^\circ$

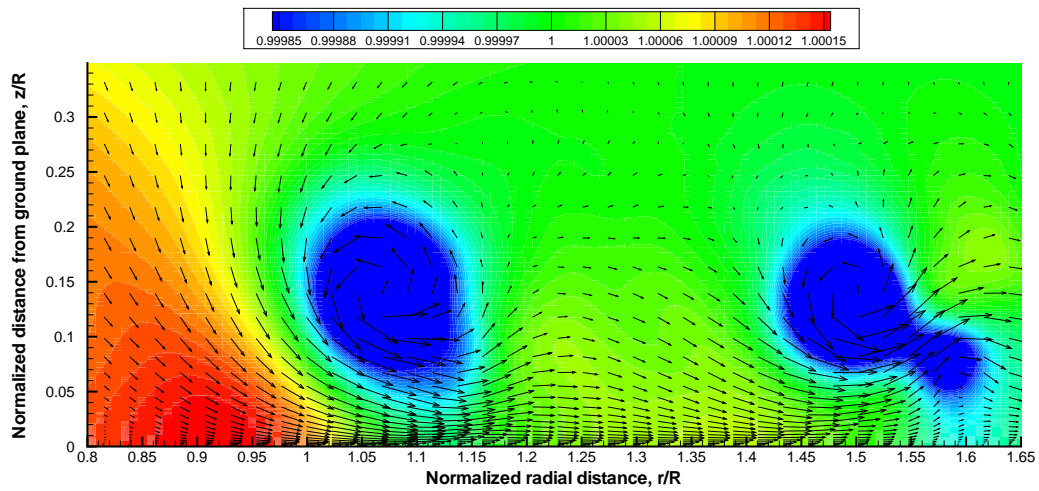
Figure 15: Velocity vectors along with pressure (non-dimensionalized by freestream value) contours for a rotor height of  $h/R = 0.5$ .



(a)  $\psi = 0^\circ$

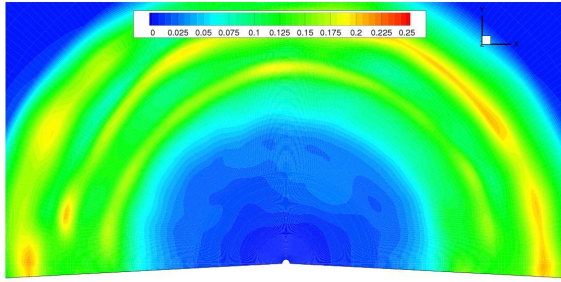


(b)  $\psi = 60^\circ$

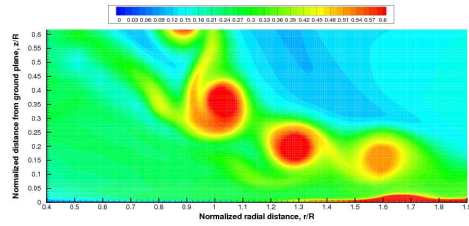


(c)  $\psi = 120^\circ$

Figure 16: Velocity vectors along with pressure (non-dimensionalized by freestream value) contours for a rotor height of  $h/R = 0.25$ .

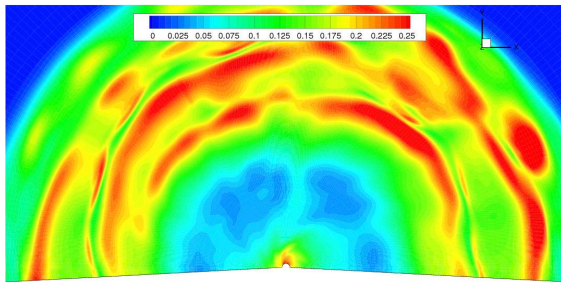


(a) Horizontal plane  $0.03R$  above ground

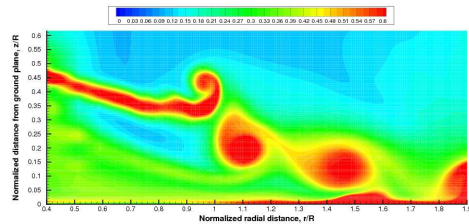


(b) Vertical plane at  $60^\circ$  wake-age

Figure 17: Contours of eddy viscosity normalized by laminar viscosity at two different planes for a rotor height of  $h/R = 1.0$ .

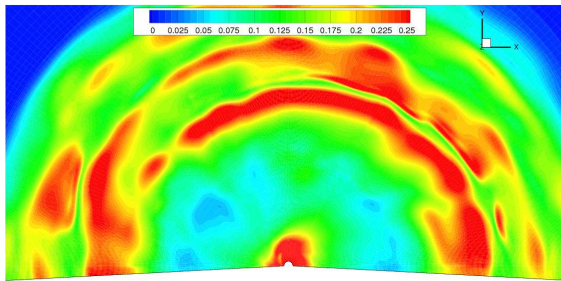


(a) Horizontal plane  $0.03R$  above ground

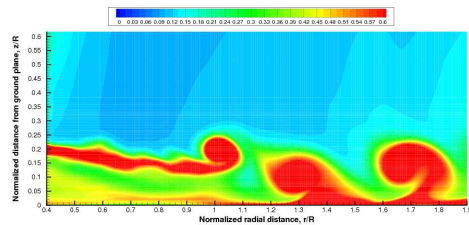


(b) Vertical plane at  $60^\circ$  wake-age

Figure 18: Contours of eddy viscosity normalized by laminar viscosity at two different planes for a rotor height of  $h/R = 0.5$ .



(a) Horizontal plane  $0.03R$  above ground



(b) Vertical plane at  $60^\circ$  wake-age

Figure 19: Contours of eddy viscosity normalized by laminar viscosity at two different planes for a rotor height of  $h/R = 0.25$ .